Journal of Computer Assisted Tomography **2013, 37(5): 770-782**

A MACRO-QUANTIFICATION APPROACH FOR REGION OF INTEREST ASSESSMENT IN EMISSION TOMOGRAPHY

F Ben Bouallègue

Abstract

In this paper we propose a quantification methodology for estimating the statistical parameters of the activity inside regions of interest (ROIs). Macro-quantification implies a rearrangement of the emission projection data into macro-projections and a redefinition of the system matrix based either on an image reconstruction involving iterative ROI-wise regularization or on an ROI uniformity assumption. The technique allows a very fast computation of the ROI activities and covariance matrix in the least squares sense using a low-dimensional model of the tomographic problem. The macro-quantification approach is evaluated through Monte-Carlo simulations using a numerical thorax phantom, without taking into account the measurement artifacts and assuming a perfect a-priori ROI definition. Various tumor ROI configurations and count rates are considered in order to reflect clinical situations. The results show that our technique yields low bias ROI estimations which turn out to be more accurate than classical estimates relying on pixel summation. Macro-quantification also provides an approximation for the ROI variance that describes the effective variance obtained through the simulations fairly well. The technique is then validated using SPECT data from a physical phantom composed of cylinders filled with different ^{99m}Tc concentrations for the task of ROI comparison. Here again, the study shows excellent agreement between the measured and predicted values of the ROI variance resulting in efficient estimations of ROI ratios and highly accurate ROI comparisons. In its simplest formulation, macro-quantification has a short computation time, making it an ideal technique for quantitative ROI assessment compatible with a wide range of routine clinical applications.

Keywords

Emission tomography, region of interest quantification, variance estimation

1. Introduction

Quantitative interpretation in emission tomography requires evaluating the uncertainty (i.e., the variance) of the reconstructed images. This is particularly true when one has to quantify or to compare the total activity inside one or several regions of interest (ROIs) having potential clinical interest. The problem of estimating image variance in emission tomography has been extensively studied. Analytical and numerical approximations have been proposed, many of them focusing on a particular reconstruction algorithm. Both filtered back-projection and maximum-likelihood algorithms have been studied since the late seventies in the field of emission tomography and many approximations have been proposed to describe the propagation of the uncertainty from the recorded data to the reconstructed images [1-21]. In 1996, Fessler drew a theoretical framework for characterizing of the variance of implicitly defined estimators which yields an approximation for the particular case of emission tomography [22]. Original methods based on bootstrapping techniques [23-24] or intervalist prediction [25-26] have also been proposed. The computation of the whole reconstructed image covariance matrix however, remains a fastidious task due to the huge dimensions (typically of $O(10^4 \times 10^4)$) of the system

matrix in classical tomographic configuration. The difficult handling of the numerical errors (resulting from the ill-conditioning of the system matrix), along with its heavy computational complexity make this task unsuitable for clinical routine. Besides, routine image interpretation requires region of interest assessment rather than pixel-wise variance estimation. Following the previous attempts to design ROI-based techniques in emission tomography [27-31], the aim of the present paper is to describe a macro-quantification approach for the computation of pre-defined ROIs activity and variance. The method allows a very fast computation of the ROI activities and covariance matrix in the least squares sense using a low-dimensional model of the tomographic problem specially dedicated to ROI study. When the ROI boundaries are accurately defined, it also provides ROI estimates that are significantly less biased than classical estimates based on pixel summation. We show that from a dimensional point of view the variance estimates provided by our method fit perfectly with the classical approximate formulations proposed by Huesman and Budinger [1-2]. The macro-quantification is first evaluated through Monte-Carlo simulations using a numerical thorax phantom with tumor-like ROIs for the estimation of the ROI statistical parameters. The technique is then validated using a physical phantom SPECT acquisition for the task of ROI comparison.

2. Materials and Methods

2.1. Classical ROI quantification

Let $\overline{\boldsymbol{\theta}} \in \mathbb{R}^{\mathrm{N}}$ be an activity distribution defined on a Cartesian grid with N the number of pixels sampling the field of view of the acquisition device. Let $\overline{\mathbf{p}} \in \mathbb{R}^{\mathrm{BD}}$ be the exact projections of $\overline{\boldsymbol{\theta}}$ where BD is the total number of recorded projections (with D the number of projection angles and B the number of bins per projection angle). Let $\boldsymbol{\Lambda} \in \mathbb{R}^{\mathrm{BD}\times\mathrm{N}}$ be the Radon operator (or system matrix) such that $\overline{\mathbf{p}} = \boldsymbol{\Lambda}\overline{\boldsymbol{\theta}}$. The system matrix component $\boldsymbol{\Lambda}_{ij}$ gives the probability for a photon emitted from pixel j to be recorded into projection i. Ideally the system matrix should perfectly model the emission/detection process, including side-effects such as auto-attenuation, Compton scattering, and detector response function. The actual recorded projections $\mathbf{p} \in \mathbb{R}^{\mathrm{BD}}$ are affected by Poisson noise, and it is commonly accepted that $Var(\mathbf{p}) \approx Diag(\mathbf{p})$ represents a good approximation of the data variance. Tomographic reconstruction intends to produce an estimator $\widehat{\boldsymbol{\theta}} \in \mathbb{R}^{\mathrm{N}}$ of the original image $\overline{\boldsymbol{\theta}}$ starting from the recorded projections $\mathbf{p}$. Most of modern reconstruction algorithms are statistical in the sense that they build up this estimator on the basis of the conditional probability of the sought after image knowing the projections. This probability is usually called the posterior $L(\boldsymbol{\theta}, \mathbf{p})$ and can be written using Baye's theorem:

$$L(\boldsymbol{\theta}, \mathbf{p}) = \wp(\boldsymbol{\theta}|\mathbf{p}) = \frac{\wp(\mathbf{p}|\boldsymbol{\theta})\,\wp(\boldsymbol{\theta})}{\wp(\mathbf{p})} \tag{1}$$

where the likelihood $\wp(\mathbf{p}|\boldsymbol{\theta})$ is such that:

$$\wp(\mathbf{p}|\boldsymbol{\theta}) = \prod_i \frac{e^{-\boldsymbol{\Lambda}\boldsymbol{\theta}_i}\,(\boldsymbol{\Lambda}\boldsymbol{\theta})_i^{\mathbf{p}_i}}{\mathbf{p}_i\,!} \tag{2}$$

The most straightforward way to design an estimator (which is also one of the most commonly used in practice) consists in searching the image that maximizes the log-posterior:

$$\widehat{\boldsymbol{\theta}} = \underset{\boldsymbol{\theta}\in\mathbb{R}^{\mathrm{N}}}{argmax}\ \left[\log\left(L(\boldsymbol{\theta}, \mathbf{p})\right)\right] \tag{3}$$

When one considers that no prior information is available concerning the reconstructed object, the probability $\wp(\boldsymbol{\theta})$ is set to constant and equation (3) defines the maximum-likelihood (ML) estimator [32-33]. No explicit formulation of this estimator can be derived and its computation is achieved using the iterative expectation-maximization algorithm (MLEM). MLEM is known to provide a low bias estimator (at least asymptotically at high count rates) for which the Cramér-Rao bound (CRB) gives a lower limit of the covariance:

$$Cov\left(\widehat{\boldsymbol{\theta}}\right) \geq \mathbf{F}^{-1} \tag{4}$$

with **F** the Fisher information matrix:

$$\mathbf{F} = E\left(-\frac{\partial^2}{\partial \boldsymbol{\theta}^2}\log\left(L(\boldsymbol{\theta},\mathbf{p})\right)\right) = \boldsymbol{\Lambda}^{\mathrm{T}}\,\mathbf{C}^{-1}\,\boldsymbol{\Lambda} \tag{5}$$

where **C** stands for the covariance matrix of the recorded data:

$$\mathbf{C} = Cov(\mathbf{p}) = Diag(\overline{\mathbf{p}}) \approx Diag(\mathbf{p}) \tag{6}$$

However, the ML estimator is known to amplify the acquisition noise through the reconstruction process, especially at low count rates [34]. Its covariance is thus highly dependent on the number of iterations after which the iterative algorithm is stopped and the CRB can no longer provide an accurate variance prediction. Besides, there exists no consensual stopping criterion allowing an optimal management of the noise-resolution tradeoff.

When dealing with ROI activities, the following notations will be employed. K will denote the number of ROIs in the studied object (usually $\mathrm{K} = 2$, i.e., one ROI plus the background). $\overline{\boldsymbol{\Psi}} \in \mathbb{R}^{\mathrm{K}}$ will denote the true activity inside the ROIs and $\widehat{\boldsymbol{\Psi}} \in \mathbb{R}^{\mathrm{K}}$ will stand for the estimator of the ROI activities. Defining $\boldsymbol{\kappa} \in \{0,1\}\mathbb{R}^{\mathrm{K}\times\mathrm{N}}$ the characteristic function of the ROIs as $\boldsymbol{\kappa}_{kj} = 1$ if pixel j is inside ROI k and $\boldsymbol{\kappa}_{kj} = 0$ otherwise, one can write:

$$\overline{\boldsymbol{\Psi}} = \boldsymbol{\kappa}\,\overline{\boldsymbol{\theta}} \tag{7}$$

The ROI estimator is usually obtained after the reconstruction process by simply summing the pixel values of the image estimator $\widehat{\boldsymbol{\theta}}$ inside the studied ROIs:

$$\widehat{\boldsymbol{\Psi}} = \boldsymbol{\kappa}\;\widehat{\boldsymbol{\theta}} \tag{8}$$

One may then use the CRB in order to compute a lower limit of the ROI estimator covariance using:

$$Cov\left(\widehat{\boldsymbol{\Psi}}\right) \geq \boldsymbol{\kappa}\,Cov\left(\widehat{\boldsymbol{\theta}}\right)\boldsymbol{\kappa}^{\mathrm{T}} \tag{9}$$

However, some critical points have to be discussed regarding this classical ROI quantification technique. When non regularized reconstruction algorithms are exploited to produce the image estimator, the bias affecting the ROI estimate is controlled by letting the algorithm reach convergence through a sufficient number of iterations. The ROI variance remains though hardly foreseeable using the CRB since the noise affecting the image estimate is strongly related to the total number of iterations (this appears clearly in our results section, Figures 5 and 6). When regularized algorithms are employed, the ROI variance amplification can be effectively subdued if correct smoothing parameters are chosen but at the price of an increase in the systematic bias. Last, from a practical point of view, the computation of the image covariance matrix using the CRB remains a hazardous task due to the huge dimensions and ill-conditioning of the system matrix to be inverted. These last considerations justify our attempt to develop an innovative formulation of the tomographic problem in a macroscopic perspective, as presented in the following section.

2.2. Macro-quantification

Classical tomographic reconstruction addresses the task of building an image using its projection data. The image is built over a Cartesian kernel constituted of pixels representing basic image elements inside

which the activity may be considered as uniform. In the particular case of emission tomography, the difficulty follows from the uneasy handling of a large system matrix $\mathbf{\Lambda}$ linking a large number of pixel values $\boldsymbol{\theta}$ with a large number of highly noisy projections $\mathbf{p}$. The huge dimensions of the linear system combined with the presence of a significant amount of noise impede a simple and efficient computation of the image estimator as well as its variance. The macro-quantification approach intends to simplify the formulation of the problem by means of a model down-sampling dedicated to ROI quantification. The studied object will be divided into K ROIs ($\mathrm{R}_k,\ k = 0 \ldots K-1$) indexed with the letter k, one being the background (ROI R_0) and the following ($\mathrm{R}_1, \mathrm{R}_2, \ldots$) being the studied ROIs themselves. These K ROIs will be considered as the basic components of the reconstructed image, acting as the pixels in classical tomography. As above, the ROI estimator will be denoted $\widehat{\boldsymbol{\Psi}} \in \mathbb{R}\mathbb{R}^{\mathrm{K}}$. In order to further reduce the system complexity, the projection data we will also be aggregated to create macro-projections denoted $\mathbf{P}$. For each projection $\mathbf{p}_i$, let us note

$$\boldsymbol{\gamma}_i = \{\mathrm{R}_{i,1}, \ldots, \mathrm{R}_{i,m}\} \ : \ \forall k, \mathrm{R}_k \in \boldsymbol{\gamma}_i \text{ if } \{\exists j \in \mathrm{R}_k \mid \mathbf{\Lambda}_{ij} > 0\} \tag{10}$$

the set of ROIs that contain at least one pixel projecting onto $\mathbf{p}_i$. Let:

$$\mathbf{\Gamma} = \{\boldsymbol{\gamma}_1, \ldots, \boldsymbol{\gamma}_{\mathrm{T}}\} \ : \ \forall (t_1, t_2)\ t_1 \neq t_2,\ \boldsymbol{\gamma}_{t_1} \neq \boldsymbol{\gamma}_{t_2} \ ; \ \forall i,\ \{\exists t, 1 \leq t \leq \mathrm{T} \mid \boldsymbol{\gamma}_i = \boldsymbol{\gamma}_t\} \tag{11}$$

be the complete set of T distinct values of $\boldsymbol{\gamma}$.

The projections are then aggregated into T macro-projections $\mathbf{P} \in \mathbb{R}\mathbb{R}^{\mathrm{T}}$**:**

$$\mathbf{P}_t = \sum_{i \mid \boldsymbol{\gamma}_i = \mathbf{\Gamma}_t} \mathbf{p}_i \tag{12}$$

Figure 1 illustrates the situation for $\mathrm{K} = 3$ ROIs. The aggregation process produces $\mathrm{T} = 4$ macro-projections using $\mathbf{\Gamma} = \{\{\mathrm{R}_0\}, \{\mathrm{R}_0, \mathrm{R}_1\}, \{\mathrm{R}_0, \mathrm{R}_2\}, \{\mathrm{R}_0, \mathrm{R}_1, \mathrm{R}_2\}\}$: $\mathbf{P}_1$ sums all the projections that only intersect the background, $\mathbf{P}_2$ those intersecting both R_0 and R_1, $\mathbf{P}_3$ those intersecting both R_0 and R_2, and $\mathbf{P}_4$ those intersecting the three ROIs. As R_1 and R_2 are located inside R_0, there is trivially no projection intersecting R_1 and/or R_2 without intersecting R_0.

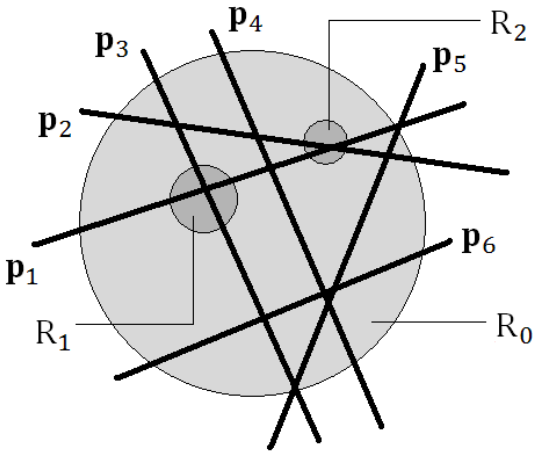

$$\mathbf{P}_1 = \mathbf{p}_4 + \mathbf{p}_5 + \mathbf{p}_6$$
$$\mathbf{P}_2 = \mathbf{p}_3$$
$$\mathbf{P}_3 = \mathbf{p}_2$$
$$\mathbf{P}_4 = \mathbf{p}_1$$

Figure 1. Aggregation of the projections into macro-projections in a 3 ROI configuration.

From the macroscopic point of view, the ROI values $\mathbf{\Psi}$ are linked with the macro-projections $\mathbf{P}$ through a linear system $\mathbf{P} = \mathbf{M}\mathbf{\Psi}$**.** The macro-projector $\mathbf{M} \in \mathbb{R}\mathbb{R}^{\mathrm{T}\times\mathrm{K}}$ is such that its element $\mathbf{M}_{tk}$ gives the probability for a photon emitted from ROI k to be detected into macro-projection t. For a given object $\overline{\boldsymbol{\theta}}$ this probability depends on the activity distribution inside the ROIs following:

$$\mathbf{M}_{tk} = \frac{\sum_{j \in \mathrm{R}_k} \sum_{i \mid \boldsymbol{\gamma}_i = \mathbf{\Gamma}_t} \mathbf{\Lambda}_{ij} \overline{\boldsymbol{\theta}}_j}{\sum_{j \in \mathrm{R}_k} \sum_i \mathbf{\Lambda}_{ij} \overline{\boldsymbol{\theta}}_j} \tag{13}$$

The Fisher information matrix $\mathbf{F}$ related to the macroscopic problem $\mathbf{P} = \mathbf{M}\boldsymbol{\Psi}$ is:

$$\mathbf{F} = \mathbf{M}^{\mathrm{T}}\, Cov^{-1}(\mathbf{P})\, \mathbf{M} \approx \mathbf{M}^{\mathrm{T}}\, Diag^{-1}(\mathbf{P})\, \mathbf{M} \quad (14)$$

As the macro-projections naturally gather a high number of events, the estimator of the ROI activities can be computed in the least squares sense using:

$$\widehat{\boldsymbol{\Psi}} = \mathbf{F}^{-1}\, \mathbf{M}^{\mathrm{T}}\, Diag^{-1}(\mathbf{P})\, \mathbf{P} \quad (15)$$

and the ROI estimator variance may hence be approximated using:

$$Cov\left(\widehat{\boldsymbol{\Psi}}\right) = \mathbf{F}^{-1} \approx [\mathbf{M}^{\mathrm{T}}\, Diag^{-1}(\mathbf{P})\, \mathbf{M}]^{-1} \quad (16)$$

Compared with the standard approach, the macroscopic approach (equations (15) and (16)) offers ROI quantification expressions that are easily computable by inverting very low dimension matrices. The produced ROI estimator is naturally unbiased and its variance is readily predictable. We show in section 2.4 below that from a dimensional point of view equation (16) produces estimates of the ROI variance that are in agreement with the classical approximations of Huesman and Budinger [1-2].

2.3. Computation of the macro-projector

In the last section, we proposed a macroscopic approach to drastically reduce the system dimensions dedicated to ROI assessment. This reduction relies on a model down-sampling from pixels to ROIs and from projections to macro-projections. The aggregation process, which affects both the data and the unknowns of the problem, inevitably induces a loss of information. The missing information is synthesized into the macro-projector which is the keystone of the macroscopic model. For a given studied object, the components of the macro-projector depend on the exact activity distribution inside the object, as defined through equation (13). In practice, the original object remains unknown and the macro-projector has to be modelled starting from the data of the problem, i.e., the recorded noisy projections. The computation of the macro-projector can be performed using equation (13) where the exact activity distribution $\overline{\boldsymbol{\theta}}$ is replaced with an image estimate $\widehat{\boldsymbol{\theta}}$:

$$\mathbf{M}_{tk} = \frac{\sum_{j\in \mathrm{R}_k} \sum_{i|\boldsymbol{\gamma}_i=\boldsymbol{\Gamma}_t} \boldsymbol{\Lambda}_{ij}\widehat{\boldsymbol{\theta}}_j}{\sum_{j\in \mathrm{R}_k} \sum_i \boldsymbol{\Lambda}_{ij}\widehat{\boldsymbol{\theta}}_j} \quad (17)$$

This estimate has to fulfil certain requirements in order to ensure sufficient accuracy and robustness of the macro-projector (Figure 2). First, this estimate has to be regularized so as to warrant the stability of the macro-projector in the presence of noise. However, if a global regularization or post-filtering of the object estimate is performed, the macro-projector will suffer from the resolution loss around the borders between the ROIs. One solution for the conjunct handling of both noise and resolution relies on an iterative ROI-wise regularization of the object estimate (similar reconstruction algorithms have already been proposed [35-37]). An MLEM scheme is employed to reconstruct the image. In between each iteration step, a convolution of the current estimated activity is performed inside each ROI with a Gaussian filter. Denoting $\mathrm{R}(j)$ the ROI containing pixel j, an iteration step is performed using:

- *MLEM update:*

$$\boldsymbol{\theta}_j^{n+1/2} = \boldsymbol{\theta}_j^n \frac{\sum_i \boldsymbol{\Lambda}_{ij} \frac{\mathbf{p}_i}{(\boldsymbol{\Lambda}\boldsymbol{\theta}^n)_i}}{\sum_i \boldsymbol{\Lambda}_{ij}} \quad (18)$$

- *ROI-wise smoothing:*

$$\boldsymbol{\theta}_j^{n+1} = \frac{\sum_{q\in \mathrm{R}(j)} G_{j,s}(q)\, \boldsymbol{\theta}_q^{n+1/2}}{\sum_{q\in \mathrm{R}(j)} G_{j,s}(q)} \quad (19)$$

where $G_{j,s}$ stands for a Gaussian kernel centered on pixel j with a standard deviation of s pixels. Using this reconstruction technique will allow the macro-projector to be accurate and robust with respect to the noise. In order to be fully efficient, this technique requires a good knowledge of the ROI boundaries so that the high activity region can be precisely discriminated from the low activity background. As the coupling of SPECT and PET acquisition with CT scanning has tended to generalize, the circumscription of the ROIs may often be performed with the help of the co-registered morphological information for an optimal computation of the macro-projector. When no morphological information is available, one has to exploit a prior image reconstruction for the definition of the ROIs. In the particular case where the defined ROIs are a-priori known to have a uniform activity distribution, one will rely on the use of the uniform macro-projector $\mathbf{U}$ which can be built naturally without preliminary image reconstruction:

$$\mathbf{U}_{tk} = \frac{\sum_{j\in \mathrm{R}_k} \sum_{i|\boldsymbol{\gamma}_i=\Gamma_t} \boldsymbol{\Lambda}_{ij}}{\sum_{j\in \mathrm{R}_k} \sum_i \boldsymbol{\Lambda}_{ij}} \tag{20}$$

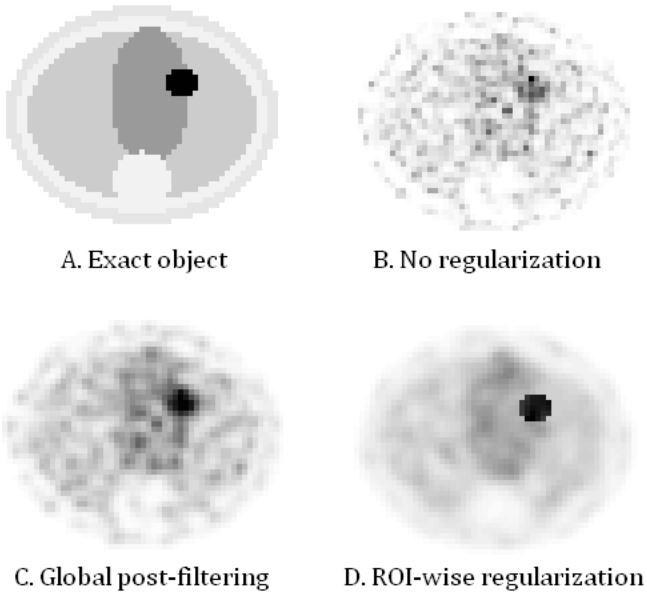

Figure 2. A: Exact object. B: MLEM 100 iterations. C: MLEM 100 iterations followed by Gaussian post-filtering of FWMH 2 pixels. D: MLEM 100 iterations with iterative ROI-wise Gaussian filtering of FWMH 1 pixel.

2.4. Dimensional study

In this section, we study the order of magnitude of the variance computed with equation (16). We assume that the recorded projections are $O(\mathrm{p})$. The image is reconstructed on a grid of dimensions $\mathrm{N} \times \mathrm{N}$. Let us consider a circular uniform ROI of diameter Δ pixels called $\mathrm{R_A}$. A second ROI $\mathrm{R_B}$ is defined as a pixel inside $\mathrm{R_A}$ (Figure 3). For each projection angle, the object projects onto $\Delta\mathrm{B}/\mathrm{N}$ bins. The total counts recorded are thus $O(\mathrm{p} \times \mathrm{D} \times \Delta\mathrm{B}/\mathrm{N})$ with p the order of magnitude of a single projection. From the fact that the total counts recorded in the projections must be recovered in the reconstructed image θ, one can infer that θ is $O\left(\frac{\text{total counts}}{\Delta^2}\right) = O\left(\frac{\mathrm{BDp}}{\mathrm{N}\Delta}\right)$.

Concerning the mean of the global activity Ψ_A inside $\mathrm{R_A}$, one has:

$$\Psi_\mathrm{A} = O(\Delta^2\theta) = O(\text{total counts}) = O\left(\frac{\Delta\mathrm{BDp}}{\mathrm{N}}\right) \tag{21}$$

As for the mean activity Ψ_B inside $\mathrm{R_B}$, one has:

$$\Psi_\mathrm{B} = O(\theta) = O\left(\frac{\mathrm{BDp}}{\mathrm{N}\Delta}\right) \tag{22}$$

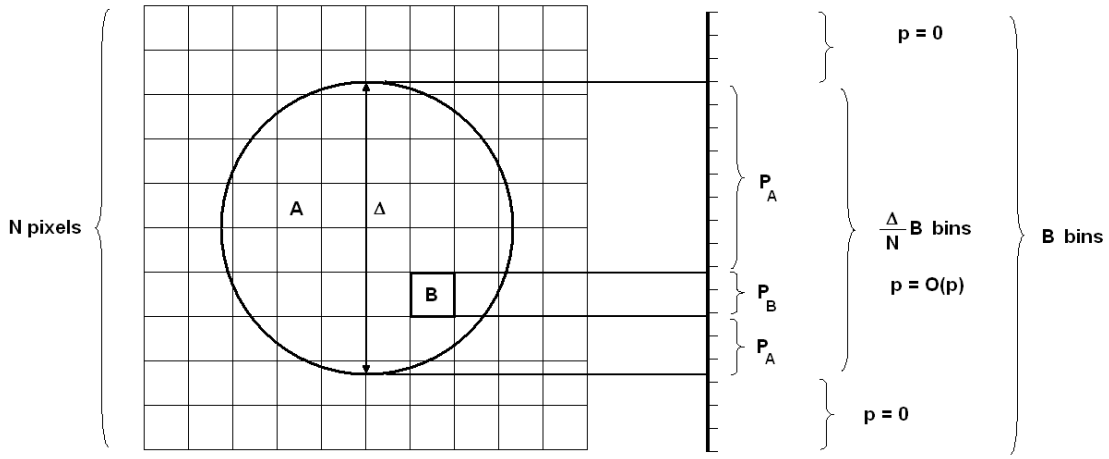

Figure 3. Case of two ROIs, one being a single pixel

One rearranges the projections into two macro-projections:

$$\overline{P}_A = O\left(\frac{\Delta BDp}{N}\right) \; ; \; \overline{P}_B = O\left(\frac{BDp}{N}\right) \tag{23}$$

Noting that the coefficients of **M** are $O(1)$ for the couples $(R_A, \overline{P}_A)$ and $(R_B, \overline{P}_B)$, and $O(0)$ for the couples $(R_A, \overline{P}_B)$ and $(R_B, \overline{P}_A)$, one computes the components of the 2□2 Fisher information matrix **F** as follows:

$$\mathbf{F}_{AA} = O\left(\frac{N}{\Delta BDp}\right) \; ; \; \mathbf{F}_{BB} = O\left(\frac{N}{BDp}\right) \; ; \; \mathbf{F}_{AB} = \mathbf{F}_{BA} = O(0) \tag{24}$$

The matrix **F** being approximately diagonal, the variance of the activities into R_A and R_B are given by:

$$\sigma_A^2 \approx \mathbf{F}_{AA}^{-1} = O\left(\frac{\Delta BDp}{N}\right) \tag{25}$$

$$\sigma_B^2 \approx \mathbf{F}_{BB}^{-1} = O\left(\frac{BDp}{N}\right) \tag{26}$$

Comparing equation (21) with equation (25), it follows that $\sigma_A^2 \approx \Psi_A$, which is in agreement with Poisson's law describing the distribution of radioactive measurement. From equations (22) and (26) one computes an estimate of the ratio σ_B/Ψ_B:

$$\frac{\sigma_B}{\Psi_B} \approx \frac{\sqrt{BDp}}{\sqrt{N}} \frac{N\Delta}{BDp} = \frac{\sqrt{p}}{p} \frac{1}{\sqrt{BD}} \Delta \sqrt{N} \tag{27}$$

which can be rewritten, provided that the object has roughly the dimensions of the field of view (i.e., $\Delta \approx N$):

$$\frac{\sigma_B}{\Psi_B} \approx \frac{\sqrt{p}}{p} \frac{1}{\sqrt{BD}} \Delta^{3/2} \tag{28}$$

Equation (28) is strictly equivalent to Huesman's formula ([1] equation (15)) which states that the ratio between the standard deviation and the mean activity of a pixel into a circular ROI can be approximated by the ratio between the standard deviation and the mean of the recorded projections, times a multiplicative factor, this factor being: (the ratio between the size of the ROI and the size of the pixel) power 3/2 divided by the square root of the total number of projections. Denoting W the number of pixels into ROI A ($W = O(\Delta^2)$), equation (27) can be rewritten as:

$$\frac{\sigma_B}{\Psi_B} = \frac{1}{\sqrt{\Psi_B}} \frac{\sigma_B}{\sqrt{\Psi_B}} \approx \frac{1}{\sqrt{\Psi_B}} \frac{\sqrt{BDp}}{\sqrt{N}} \sqrt{\frac{N\Delta}{BDp}} = \frac{\sqrt{\Delta}}{\sqrt{\Psi_B}} \approx \frac{W^{1/4}}{\sqrt{\Psi_B}} \tag{29}$$

which is in agreement with Budinger's approximation [2].

3. Results

3.1. Monte-Carlo simulations

We studied a numerical phantom modelling a thorax slice. The phantom was constituted of four tissues (bone, fat, lung and mediastinum) with different activities (Figure 4 top and Table 1) representing the background, i.e., ROI 0. We simulated three two-ROI configurations. The ROIs stood for chest tumors with various locations, sizes and relative uptakes with respect to the background (Figure 3 bottom and Table 2).

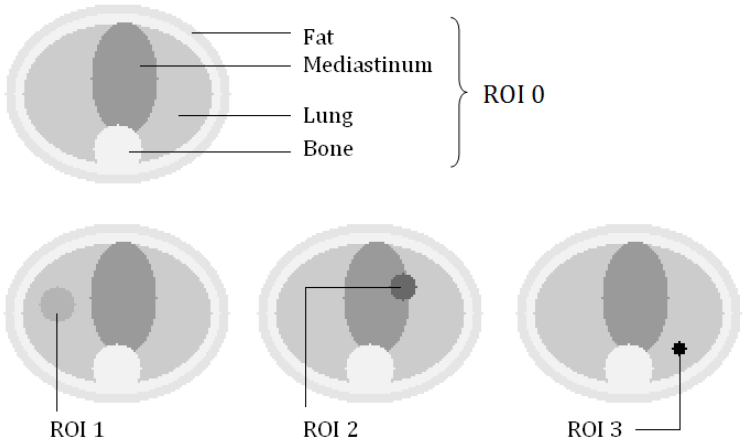

Figure 4. *Top*: the studied numerical phantom. *Bottom*: the three studied tumor ROI configurations.

Table 1. Composition of the numerical thorax phantom

Tissue	Relative uptake
Bone	1
Fat	2
Lung	4
Mediastinum	8

Table 2. Characteristics of the ROIs

Tumor region of interest	Radius	Relative uptake
ROI 1	8 pixels	6
ROI 2	6 pixels	12
ROI 3	3 pixels	20

The object was defined and reconstructed on a 128 × 128 grid. Its projections were simulated using 128 projection angles over 180° and 128 bins per projection angle, without taking into account the scatter or attenuation and assuming a perfect detector response. When simulating realistic noisy records, Poisson noise was added using Knuth's algorithm [38]. The coefficients of the Radon matrix $\mathbf{\Lambda}$ were computed using a uniformly distributed pixel activity model. Two count rates were considered: 25,000 events and 400,000 events (on average). For each count rate, 250 realistic noisy replicates of the projection data were simulated and exploited to estimate the ROI parameters using different methodologies. The first evaluated methodology was the macro-quantification technique. The macro-projector was computed on the basis of an image estimate produced using MLEM with iterative ROI-wise regularization. The

regularization was performed by filtering the image after each iteration, ROI by ROI, with a Gaussian kernel of full width at mid-height (FWMH) 1 pixel. During image reconstruction, at each iteration, the macro-projector was computed and equations (15) and (16) were employed to provide an estimation of the ROI activity and variance. In what follows, the ROI estimation obtained with this technique (equation (15)) will be denoted Macro-Q. The macro-estimate of the ROI standard deviation (square root of the variance predicted using equation (16)) will be called Macro-σ. Our methodology was compared with a standard technique for ROI assessment which consists in reconstructing an estimate of the object using classical MLEM (with and without a-posteriori regularization) and then summing the pixel values inside the considered ROI (equation (8)). This was done using the following parameters:

- MLEM without regularization, refered to as $MLEM_{NR}$.
- MLEM followed by post-filtering using a Gaussian kernel of FWMH 1 pixel, refered to as $MLEM_{PF1}$.
- MLEM followed by post-filtering using a Gaussian kernel of FWMH 2 pixels, refered to as $MLEM_{PF2}$.

The three two-ROI configurations proposed in Figure 4 were processed separately and independently. For each configuration and each count rate, the four methods presented here above were run for a total of 150 iterations. During the iterative process, each of the four methodologies provided a set of 250 estimations of the ROI value (Macro-Q, $MLEM_{NR}$, $MLEM_{PF1}$ and $MLEM_{PF2}$) corresponding to the 250 replicates of the projection data. Furthermore, the macro-quantification technique allowed the computation of 250 estimates of the ROI standard deviation (Macro-σ). Figure 5 presents the results obtained for the three ROI configurations after the 25,000 event simulations. The bottom curves show the evolution with the number of iterations of the mean of the four ROI estimators. Macro-Q is displayed using a thick line, $MLEM_{NR}$ using a thin line, $MLEM_{PF1}$ using a dashed line and $MLEM_{PF2}$ using a dotted line. The straight gray line stands for the true ROI value. The top curves show the evolution with the iterations of the standard deviation of the four ROI estimators. The correspondence between the line type and the method is the same as for the bottom curves. The gray area represents the evolution with the iterations of the range ([min max]) of the Macro-σ predictions.

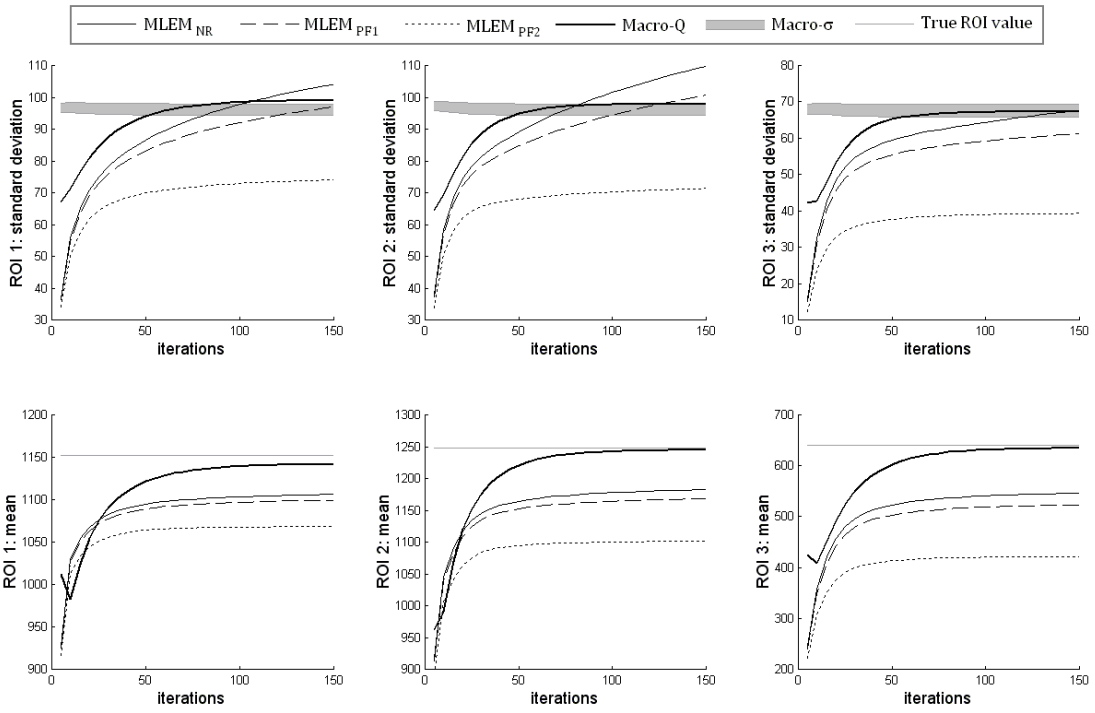

Figure 5. Results for the 25,000 event Monte-Carlo simulations. *Top*: standard deviation of the ROI value estimates along with the iterations. *Bottom*: mean of the ROI value estimates along with the iterations. *Left to right*: ROI 1, ROI 2, and ROI 3.

Figure 6 is the counterpart of Figure 5 for the 400,000 event simulations. Finally, Table 3 summarizes the quantitative results provided by the macro-quantification technique for each ROI configuration and count rate. The proposed results correspond to a total of 150 iterations, when the method can be considered as having reached convergence.

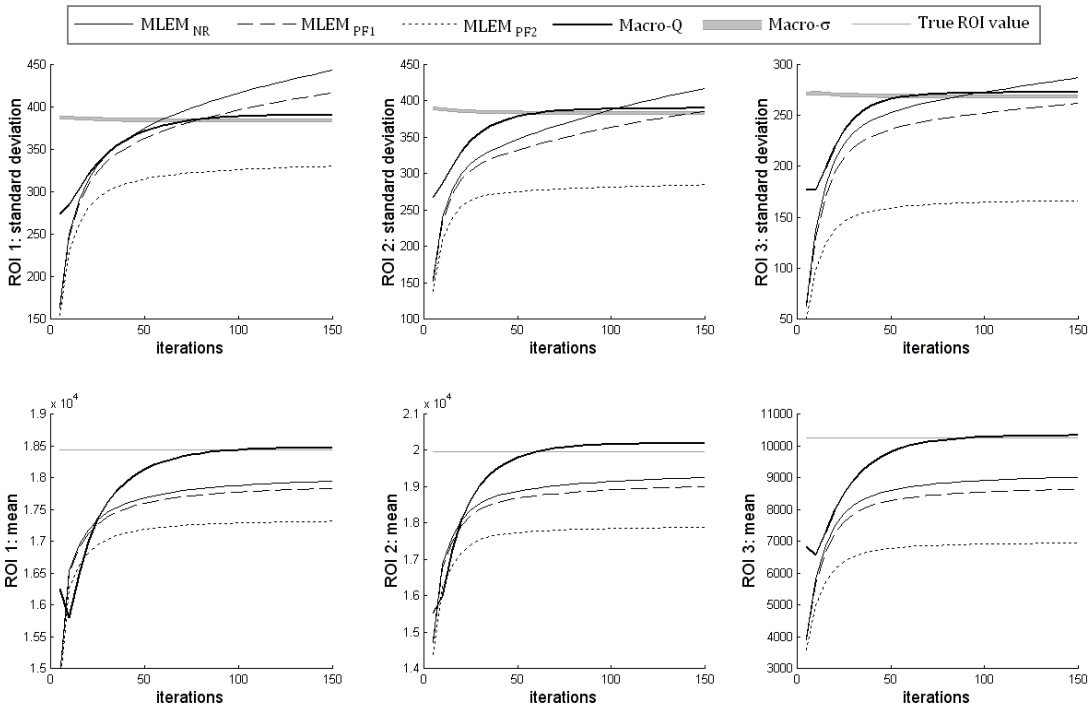

Figure 6. Same as Figure 4 for the 400,000 event Monte-Carlo simulations.

Table 3. Monte-Carlo simulations. Quantitative results for the macro-quantification of the ROI values (values at convergence: 150 iterations).

ROI number	Average count rate	True ROI value	Macro-Q mean	Relative bias	Absolute bias	Macro-Q std. dev.	Macro-σ [min max]	Relative error
1	25,000	1152	1142	- 0.9 %	- 10	99	[94 98]	[-5 -1] %
	400,000	18432	18472	+ 0.2 %	+ 40	391	[382 386]	[-2 -1] %
2	25,000	1248	1245	- 0.2 %	- 3	98	[94 98]	[-4 0] %
	400,000	19968	20193	+ 1.1 %	+ 225	390	[382 386]	[-2 -1] %
3	25,000	640	634	- 0.9 %	- 6	67	[66 69]	[-1 +3] %
	400,000	10240	10322	+ 0.8 %	+ 82	272	[267 270]	[-2 -1] %

3.2. Physical phantom study

The studied physical phantom was composed of a big cylinder of length L = 54.9 cm and diameter B = 40.2 cm containing three angularly evenly spaced small cylinders of diameter S = 12.4 cm located at a distance d = 8.5 cm from the big cylinder axis (Figure 7). The big cylinder was filled with water. The three small cylinders were filled with ^{99m}Tc solutions with various activities: cylinder 1 (C_1) was filled with 1.5 mCi/L, cylinder 2 (C_2) with 1.25 mCi/L, and cylinder 3 (C_3) with 1 mCi/L. A tomographic record of the physical phantom was acquired with an Infinia Hawkeye 4 SPECT-CT dual-head gamma-camera (GE Healthcare, Chalfont St. Giles, UK) using the following settings: projection sampling 128×128 corresponding to a resolution of 4.42×4.42 mm², 120 projection angles over 360°, and an acquisition time of 15 seconds per projection angle. A total of 90 2D sinograms were recorded,

corresponding to 90 transaxial slices of the phantom. Each 2D sinogram was corrected for Compton scattering by means of the Jaszczak method. At this point, the total number of recorded photons in the 2D sinograms exhibited a clear discordance between the internal slices and the external slices due to a significant difference in the amount of para-axial scattering affecting the internal and external slices.

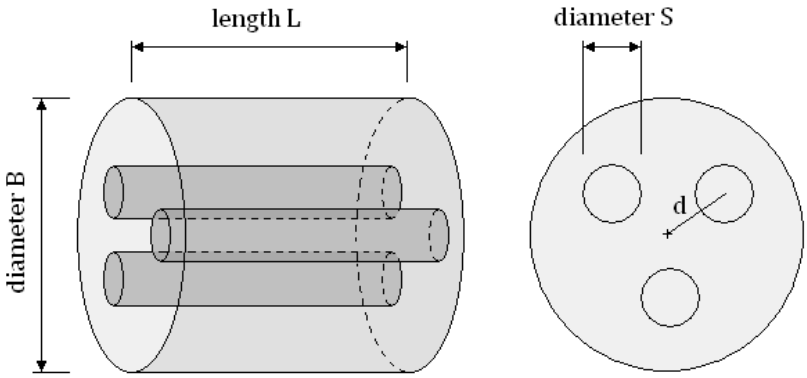

Figure 7. Geometry of the physical phantom: L = 59.4 cm, B = 40.2 cm, S = 12.4 cm, d = 8.5 cm.

In order to produce projection data corrected for this bias, we proceeded as follows: the 90 2D sinograms were summed to create a global 120×128 2D sinogram gathering 8.12 million events (Figure 8). This high statistics global sinogram was then used to generate two sets of low statistics sinograms:

- The first set is constituted of 400 low-count sinograms with an approximate average count rate per sinogram of about 20,000.
- The second set is constituted of 400 high-count sinograms with an approximate average count rate per sinogram of about 100,000.

Figure 8. The high statistics global 2D sinogram of the physical phantom.

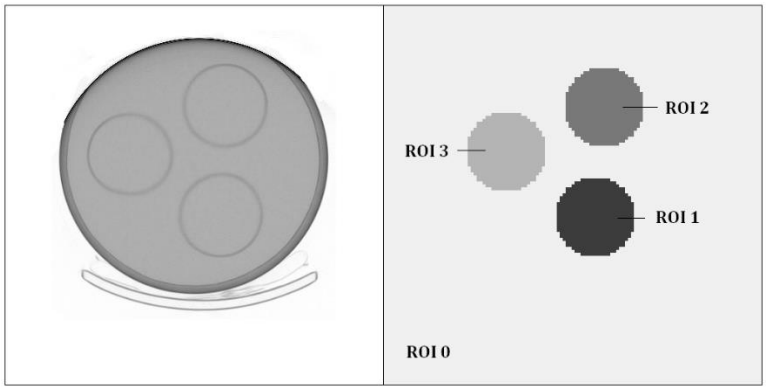

Figure 9. *Left*: CT scan slice of the physical phantom. *Right*: defined regions of interest.

A sinogram *S* of the first set was produced as follows: *S* was initialized as an identically null 120×128 matrix. Then the global sinogram was swept through and each of the 8.12 million events had a probability $p = 1/400$ to be affected to the low count sinogram *S* at the position (i,j) where it was recorded in the global sinogram. Similarly, a sinogram of the second set was produced using the same scheme with a probability $p = 1/80$. The emission images were reconstructed over a 128×128 grid. The coefficients of the system matrix were built up using the intersection area method and a uniform pixel

model. The Infinia Hawkeye 4 gamma-camera was coupled with a CT scanner that allowed the acquisition of a morphological density scan of the phantom. The CT reconstructed image was sampled on a 128×512×512 grid. After down-sampling to 128×128 in order to fit with the SPECT reconstruction kernel dimensions, the CT image enabled the definition of four ROIs (background plus three circular ROIs), the numbering of the ROIs corresponding to the numbering of the cylinders (Figure 9). Besides, the CT density map allowed the correction of the system matrix components in order to account for auto-attenuation.

We first focused on the estimation of the activity ratios between the ROIs. The ratio between ROI 1 and ROI 2 (denoted ρ_{12}) is expected to be equal to 120%, the ratio between ROI 1 and ROI 3 (denoted ρ_{13}) is expected to be equal to 150%, and the ratio between ROI 2 and ROI 3 (denoted ρ_{23}) is expected to be equal to 125%. Each sinogram was evaluated in terms of these three ratios using the macro-quantification technique. The four ROIs were processed all together. The macro-quantification was run using a uniform macro-projector as defined in equation (20). This was legitimated by our a-priori knowledge regarding the uniformity of the studied ROIs. In this case, no image needed to be reconstructed and the technique gave a punctual estimate of the following parameters:

- ROI values (Macro-Q for ROI 1, 2 and 3).
- ROI covariance matrix, from which the ROI standard deviations (Macro-σ for ROI 1, 2 and 3) are extracted.
- ROI ratios (Macro-Q for ρ_{12}, ρ_{13} and ρ_{23}).
- ROI ratios standard deviation (Macro-σ for ρ_{12}, ρ_{13} and ρ_{23}).

Equations (15) and (16) were employed to provide an estimation of the ROI values and covariance matrix. The ROI ratios were produced by simply computing the quotient of the corresponding ROI values:

$$\text{Macro\_Q}(\rho_{mn}) := \frac{\widehat{\boldsymbol{\Psi}}_m}{\widehat{\boldsymbol{\Psi}}_n} \tag{30}$$

where m and n stand for the indices of the two concerned ROIs. The macro-estimate of the standard deviation of the ROI ratios was then computed from the ROI values and covariance matrix using:

$$\text{Macro\_}\sigma(\rho_{mn}) = \frac{\sqrt{\widehat{\boldsymbol{\Psi}}_n^2\, Cov_{mm}(\widehat{\boldsymbol{\Psi}}) + \widehat{\boldsymbol{\Psi}}_m^2\, Cov_{nn}(\widehat{\boldsymbol{\Psi}}) - \widehat{\boldsymbol{\Psi}}_m \widehat{\boldsymbol{\Psi}}_n\, Cov_{mn}(\widehat{\boldsymbol{\Psi}})}}{\widehat{\boldsymbol{\Psi}}_n^2} \tag{31}$$

where m and n stand for the indices of the two concerned ROIs. Table 4 summarizes the quantitative results provided for ROI ratio estimation.

Table 4. Physical phantom study. Quantitative results for the macro-quantification of the ROI ratios.

ROI ratio	Average count rate	True ratio	Macro-Q mean	Relative bias	Absolute bias	Macro-Q std. dev.	Macro-σ [min max]	Relative error
ρ_{12}	100,00	1.2	1.25	+ 4.2 %	+ 0.05	11.6 10^{-3}	[11.2 12.0] 10^{-3}	[-3 +3] %
	20,000	1.2	1.25	+ 4.2 %	+ 0.05	25.7 10^{-3}	[23.9 27.9] 10^{-3}	[-7 +9] %
ρ_{13}	100,00	1.5	1.46	- 0.7 %	- 0.01	14.9 10^{-3}	[14.4 15.6] 10^{-3}	[-3 +5] %
	20,000	1.5	1.46	0 %	- 0.00	33.6 10^{-3}	[31.2 36.2] 10^{-3}	[-7 +8] %
ρ_{23}	100,00	1.25	1.22	- 4.0 %	- 0.05	13.4 10^{-3}	[12.9 13.9] 10^{-3}	[-4 +4] %
	20,000	1.25	1.22	- 4.0 %	- 0.05	30.8 10^{-3}	[28.3 32.9] 10^{-3}	[-8 +7] %

A second series of calculations was then performed in order to determine to what extent the macro-quantification method enabled correct comparisons between regions of interest. Random pairs of sinograms were considered. Let us denote with $(\Psi_{n,1}, V_{n,1})$ and $(\Psi_{n,2}, V_{n,2})$ the corresponding pair of macro-estimates of the ROI value and variance for ROI n. The tested null hypothesis was the following:

$$H_0: \Psi_{n,1} = \Psi_{n,2} \quad \Leftrightarrow \quad \delta_n \triangleq \Psi_{n,1} - \Psi_{n,2} = 0 \tag{32}$$

The corresponding z-score was computed as:

$$\varepsilon_n = \frac{\Psi_{n,1} - \Psi_{n,2}}{\sqrt{V_{n,1} + V_{n,2}}} \tag{33}$$

In each sinogram set, 1000 random pairs were processed, providing 1000 samples for the distributions ε_n $(n = 1 \ldots 3)$. On the basis of the z-score distribution, we deduced for each set and each ROI number four statistical indicators:

- N_95 the proportion of sinogram pairs for which the two ROIs were considered as having equal value with a first-order risk of 5%.
- N_90 the proportion of sinogram pairs for which the two ROIs were considered as having equal value with a first-order risk of 10%.
- N_80 the proportion of sinogram pairs for which the two ROIs were considered as having equal value with a first-order risk of 20%.
- N_50 the proportion of sinogram pairs for which the two ROIs were considered as having equal value with a first-order risk of 50%.

Figure 10 displays the histograms of the z-scores ε_n $(n = 1 \ldots 3)$ for the two sinogram sets. For comparison, the standard normal distribution is superimposed on each subplot. Finally, Table 5 summarizes the quantitative values of the four aforementioned indicators for each ROI and each count rate.

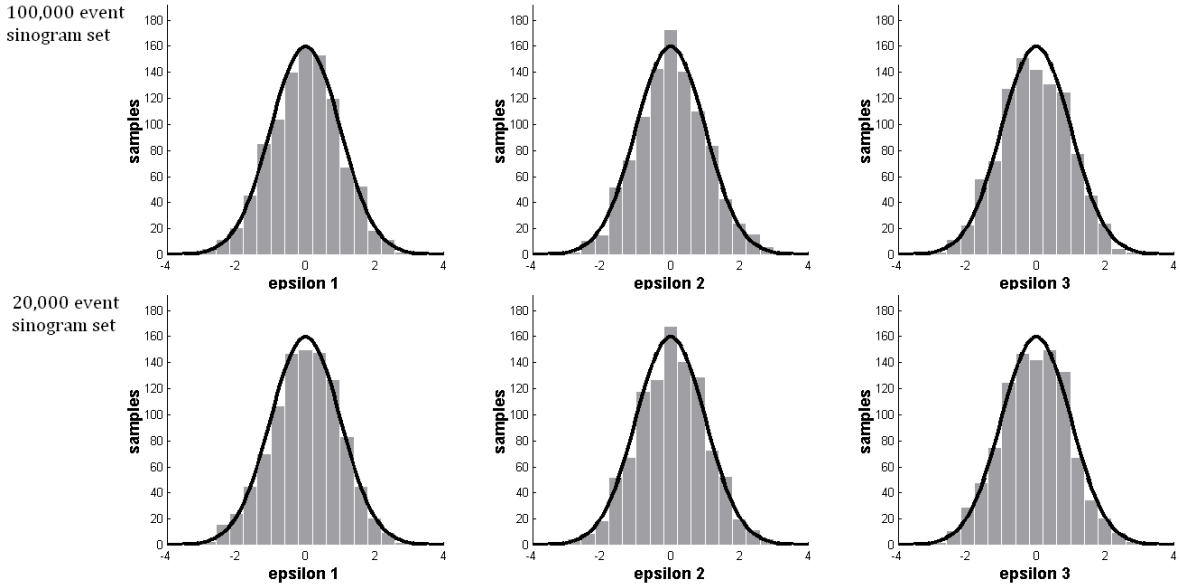

Figure 10. Physical phantom study. Histograms of the z-scores. *Top*: 100,00 event sonogram set. *Bottom*: 20,00 event sonogram set. *From left to right*: z-scores ε_1, ε_2 and ε_3. The curve of the standard normal distribution is superimposed.

Table 5. Physical phantom study. Statistical indicators for ROI comparison.

ROI	Count rate	N_95	N_90	N_80	N_50
	100,00	94.3 %	89.1 %	80.3 %	49.7 %
1	20,000	94.6 %	89.1 %	78.1 %	50.7 %
	100,00	94.6 %	90.1 %	78.2 %	48.1 %
2	20,000	94.0 %	90.1 %	79.5 %	50.4 %
	100,00	95.1 %	89.5 %	80.5 %	49.5 %
3	20,000	95.7 %	89.9 %	78.9 %	47.7 %

4. Discussion

4.1. Monte-Carlo simulations

Foremost, a few points have to be highlighted regarding the validation settings. First, a thorax phantom was chosen to evaluate the methodology on a realistic working case involving a tumor region of interest located inside a highly non-uniform background. The non-uniformity of the background allows evaluating the ability of the technique to produce an accurate macro-projector. Three ROI configurations were tested in the same perspective. Indeed, the macro-projector estimate has to show good accuracy whatever the ROI size, relative uptake or location. One of the ROI configurations involves a tumor located astride two background structures with different activities in order to evaluate the behavior of the quantification technique in this particularly common case. Second, it was decided not to take into account the classical measurement artifacts affecting the projections in emission tomography. All of these artifacts can be modelled inside the system matrix $\mathbf{\Lambda}$ whenever this is necessary using classical data corrections as presented elsewhere [39]. The imprecision affecting the system matrix components would equally affect any ROI assessment methodology by inducing a systematic bias in the ROI estimates. In order to judge the intrinsic qualities of macro-quantification versus classical quantification methods, the same operator was used for data simulation and image reconstruction, assuming the ideal case of a perfect modelling of the system matrix. Last, the boundaries of the studied ROIs were considered as perfectly defined. This is justified by the fact that a CT image is increasingly available along with the SPECT or PET data allowing precise circumscription of the ROIs on a morphological basis. Moreover, the problem of ROI definition is linked to a segmentation issue beyond the scope of the present paper.

The results presented in the previous section tend to be relatively homogenous, whatever the ROI configuration and count rate. Concerning classical ROI quantification using MELM and pixel summation, Figures 5 and 6 (bottom curves) show that the ROI estimates are affected by a systematic bias caused by partial volume effects at the border of the ROI. The mean of the estimates asymptotically converges toward a limit which always underestimates the true ROI value. As expected, this underestimation increases when post-filtering is applied and is correlated with the width of the post-filtering kernel. Concerning the variability of the classical ROI estimates, Figures 5 and 6 (top curves) indicate that the standard deviation gradually rises with the number of iterations, without stabilizing. When strong post-filtering ($MLEM_{PF2}$) is applied, the variance of the estimates tends to reach a plateau but at the price of a major bias. These last considerations emphasize the difficulty to find an optimal bias/variance tradeoff using classical ROI quantification.

As for the macro-quantification approach, Figures 5 and 6 demonstrate that it allows a good tradeoff between systematic bias and variance. The bottom curves show that the convergence of the mean value of Macro-Q toward the true ROI value is rather satisfying and always significantly better than with the

classical method. This is supported by the quantitative results summarized in Table 3: the relative bias affecting the Macro-Q estimates never exceeds 1.1 % at convergence. This superiority of the macroscopic approach over the classical method follows from a better handling of partial volume effects at the edges of the ROI. When passing from the pixel model to the macroscopic model, the sensitivity of the system matrix to partial volume effects dramatically decreases. Regarding the variability of the Macro-Q estimates, Figures 5 and 6 (top curves) show that their standard deviation always reaches a plateau during the iterative process. Furthermore, the plateau value is fairly well approximated by the Macro-σ estimate. As shown in Table 3, the Macro-σ estimates have very low dispersion with a relative error that never exceeds 5 % (Macro-σ mostly underestimates the effective standard deviation). Moreover, it appears that the systematic bias is always significantly lower than the standard deviation, which means that the unknown error (i.e., the bias) remains small compared with the controlled error (i.e., the statistical uncertainty fairly well approximated with Macro-σ).

4.2. Physical phantom study

The physical phantom study evaluated the macro-quantification technique in the frame of ROI comparison. The a-priori assumption regarding the uniformity of the ROIs allowed exploiting the simple formulation based on the uniform macro-projector. A first series of calculations tested the ability of the method to estimate the expectation and variance of the activity ratio between two regions of interest. The results shown in Table 4 demonstrate the good ability of macro-quantification to recover the exact values of the ROI ratios, with a relative bias always lower than 5 %. The observed bias is likely due to a resolution loss induced by the extraction of the ROI boundaries on a 128×128 kernel using the 512×512 CT image. Concerning the dispersion indicators, Tables 4 shows a very good agreement between the Macro-Q standard deviations and the Macro-σ predictions: the relative error ranges from -4% to +5% for the 100,000 event sinogram set and from -8% to +9% for the 20,000 event sinogram set.

A second series of calculations was carried out to assess the efficiency of macro-quantification in ROI comparison. A statistical test was applied to pairs of ROIs having theoretically equal activity levels. Figure 10 shows that the computed z-score histograms perfectly fit with the expected standard normal distribution. Accordingly, the statistical indicators presented in Table 5 show perfect agreement with the expected values of 95%, 90%, 80% and 50%, whatever the studied ROI and count rate. The physical phantom study thereby confirms the ability of macro-quantification to provide robust and accurate estimates of ROI statistical parameters in realistic working conditions (approximate knowledge of the system matrix and a-posteriori circumscription of the ROIs using morphological information). Whenever this is necessary for clinical decision, the accuracy of the Macro-σ predictions is broadly sufficient to provide a helpful insight into the order of magnitude of the ROI (or ROI ratio) variance. As discussed, the quality of the variance estimate allows for efficient comparisons between regions of interest using classical statistical tests. When the studied ROIs are a-priori known to be homogenous, which is current in routine practice (striatal neurodopaminergic imaging for instance [40]), the use of the uniform macro-projector enables an extremely fast computation of the ROI parameters (less than 1 second on a personal computer) without involving any image reconstruction. This should be particularly helpful in the frame of dynamic imaging implying ROI quantification together with low statistics data and stringent time-management constraints.

5. Conclusion

In this paper, we described an innovative methodology for the statistical characterization of regions of interest. The cornerstone of the technique is the rearrangement of the projection data into macro-projections that are linked to the ROI activities through a macro-projector. We proposed a strategy for

the computation of the macro-projector using iterative image reconstruction coupled with ROI-wise smoothing. We first evaluated the results of the methodology through Monte-Carlo simulations based on a thorax phantom and involving various tumor ROI configurations and count rates compatible with clinical practice. For the sake of convenience and in order to judge the intrinsic ability of the method to quantify ROI activities, the measurement artifact affecting the projection data were neglected and a perfect a-priori definition of the ROIs was considered. The results indicated that macro-quantification allows an optimal handling of the ROI statistical parameters. The provided ROI estimations significantly reduced the systematic bias compared with classical ROI assessment, and the variance estimation produced by the macroscopic approach fairly well agreed with the effective variance of the macroscopic ROI estimates. Next, we validated the new methodology using SPECT data of a physical phantom. The task was to compare three regions of interest defined on the basis of a co-registered CT image. Here again, the bias affecting the ROI ratio estimates was almost negligible and always below 5% of the true ROI ratio. The ratio variance estimates targeted fairly well the order of magnitude of the measured variances, with a maximum relative error ranging from about 5% for the high count sinograms to about 10 % for the low count ones. The quality of these variance estimations allowed highly accurate ROI comparisons using standard statistical decision tests. Owing to its intrinsic simplicity, the macro-quantification approach allows fast computations compatible with a wide range of routine clinical applications.

References

[1] R. H. Huesman, "Effects of a Finite Number of Projection Angles and Finite Lateral Sampling of Projections on the Propagation of Statistical Errors in Transverse Section Reconstruction". *Phys. Med. Biol.*, vol. 22-3, pp. 511-521, 1977.

[2] T. F. Budinger, S. E. Derenzo, G. T. Gullberg, W. L. Greenberg, L. William and R. H. Huesman, "Emission Computer Assisted Tomography with Single-Photon and Positron Annihilation Photon Emitters". *Journal of Computer Assisted Tomography*, vol. 1-1, pp. 131-145, 1977.

[3] N. M Alpert, D. A. Chesler, J. A. Correia, R. H. Ackerman, J. Y. Chang, S. Finklestein, S. M. Davis, G. L. Brownell and J. M. Taveras, "Estimation of the Local Statistical Noise in Emission Computed Tomography". *IEEE Trans. Med. Imag.*, vol. 1-2, pp. 142-146, 1982.

[4] D. L. Snyder, M. I. Miller, L. J. Thomas and D. G. Politte, "Noise and Edge Artifacts in Maximum-Likelihood Reconstructions for Emission Tomography". *IEEE Trans. Med. Imag*., vol 6-3, pp. 228-238, 1987.

[5] S. C. Moore, M. F. Kijewski, S. P. Müller and B. L. Holman, "SPECT Image Noise Power: Effects of Nonstationary Projection Noise and Attenuation Compensation". *J. Nucl. Med.*, vol. 29-10, pp. 1704-1709, 1988.

[6] G. J. Gillen, "A Simple Method for the Measurement of Local Statistical Noise Levels in SPECT". *Phys. Med. Biol*., vol. 37-7, p. 1573, 1992.

[7] M.J. Tapiovaara and R. F. Wagner, "SNR and Noise Measurement for Medical Imaging: I. A Practical Approach Based on Statistical Decision Theory". *Phys. Med. Biol.*, vol. 38-1, pp. 71-92, 1993.

[8] M.J. Tapiovaara, "SNR and Noise Measurement for Medical Imaging: II. Application to fluoroscopic x-ray equipment". *Phys. Med. Biol.*, vol. 38-12, pp. 1761-1788, 1993.

[9] D. W. Wilson and B. W. Tsui, "Noise Properties of Filtered-Backprojection and ML-EM Reconstructed Emission Tomography Images". *IEEE Trans. Nucl. Sc.*, vol. 40-4, pp. 1198-1203, 1993.

[10] S. C.Liew, B. H. Hasegawat, J. K. Brown and T. F. Lang, "Noise Propagation in SPECT Images Reconstructed Using an Iterative Maximum-Likelihood Algorithm". *Phys. Med. Biol.,* vol. 38, pp. 1713-1726, 1993.

[11] H-J. Kim, B. R. Zeeberg and R. C. Reba, "Evaluation of Reconstruction Algorithms in SPECT Neuroimaging: I. Comparison of Statistical Noise in SPECT Neuroimages with 'Naive' and 'Realistic' Predictions". *Phys. Med. Biol*., vol. 38, pp. 863-873, 1993.

[12] H-J. Kim, B. R. Zeeberg and R. C. Reba, "Evaluation of Reconstruction Algorithms in SPECT Neuroimaging: II. Computation of Deterministic and Statistical Error Components". *Phys. Med. Biol*., vol. 38, pp. 881-895, 1993.

[13] H. H. Barrett, D. W. Wilson and B. M. Tsui, "Noise Properties of the EM Algorithm: I. Theory". *Phys. Med. Biol.,* vol. 39, pp. 833-846, 1994.

[14] H. H. Barrett, D. W. Wilson and B. M. Tsui, "Noise Properties of the EM Algorithm: II. Monte-Carlo Simulations". *Phys. Med. Biol.,* vol. 39, pp. 847-872, 1994.

[15] X. Pan and C. E. Metz, "Analysis of Noise Properties of a Class of Exact Methods of Inverting the 2-D Exponential Radon Transform". *IEEE Trans. Med. Imag*., vol. 14-4, pp. 659-668, 1995.

[16] W. Wang and G. Gindi, "Noise Analysis of MAP-EM Algorithms for Emission Tomography". *Phys. Med. Biol.,* vol. 42-11, pp. 2215-2232, 1997.

[17] D. J. Kadrmas, E. V. R. DiBella, R. H. Huesman and G. T. Gullberg, "Analytical Propagation of Errors in Dynamic SPECT: Estimators, Degrading Factors, Bias and Noise". *Phys. Med. Biol.,* vol. 44, pp. 1997-2014, 1999.

[18] Q. Jinyi and R. M. Leahy, "Fast computation of the Covariance of MAP Reconstructions of PET Images". *SPIE Proceedings Series*, vol. 3661-2, pp 344-355, 1999.

[19] J. Nuyts, "On Estimating the Variance of Smoothed MLEM Images". *IEEE Trans. Nucl. Sc.,* vol. 40-3, pp. 714-721, 2002.

[20] D. Mariano-Goulart, M. Fourcade, J. L. Bernon, M. Zanca and M. Rossi, "Experimental Study of Stochastic Noise Propagation in SPECT Images Reconstructed Using the Conjugate Gradient Algorithm". *Comp. Med. Imag. Graph.,* vol. 27, pp. 53-63, 2003.

[21] L. D. Nickerson, S. Narayana, L. Lancaster, P. T. Fox and J-H. Gao, "Estimation of the Local Statistical Noise in Positron Emission Tomography Revisited: Practical Implementation". *Neuroimage,* vol. 19, pp. 442-456, 2003.

[22] J. A. Fessler, "Mean and Variance of Implicitly Defined Biased Estimators (Such as Penalized Maximum Likelihood): Applications to Tomography". *IEEE Trans. Image. Proc.*, vol. 5-3, pp. 493-506, 1996.

[23] D. R. Haynor, S. D. Woods, "Resampling Estimates of Precision in Emission Tomography". *IEEE Trans. Med. Imag*., vol. 8-4, pp. 337-343, 1989.

[24] I. Buvat, "A Bootstrap Approach for Analyzing the Statistical Properties of SPECT and PET Images". *Phys. Med. Biol.*, vol. 47-10, pp. 1761-1775, 2002.

[25] A. Rico, O. Strauss and D. Mariano-Goulart, "Choquet integrals as projection operators for quantified tomographic reconstruction". *Fuzzy Sets and Systems*, vol. 160-2, pp. 198-211, 2009.

[26] O. Strauss, A. Lahrech, A. Rico, D. Mariano-Goulart and B. Telle, "NIBART: A New Interval Based Algebraic Reconstruction Technique for Error Quantification of Emission Tomography Images". *Medical Image Computing and Computer-Assisted Intervention - MICCAI*, 2009.

[27] R. H. Huesman, "A New Fast Algorithm for the Evaluation of Regions of Interest and Statistical Uncertainty in Computed Tomography". *Phys. Med. Biol.*, vol. 29-5, p. 543, 1984.

[28] R. E. Carson, "A Maximum Likelihood Method for Region-of-Interest Evaluation in Emission Tomography". *Journal of Computer Assisted Tomography*, vol. 10-4, pp. 654-663, 1986.

[29] A. R. Formiconi, "Least Squares Algorithm for Region-of-Interest Evaluation in Emission Tomography". *IEEE Trans. Med. Imag*., vol. 1-1, pp. 90-100, 1993.

[30] R. E. Carson, Y. Yan, M. E. Daube-Witherspoon, N. Freedman, S. L. Bacharach, P. Herscovitch, "An Approximation Formula for the Variance of PET Region-of-Interest Values". *IEEE Trans. Med. Imag.*, vol. 12-2, pp. 240-250, 1993.

[31] E. Vanzi, M. T. De Cristofaro, S. Ramat, B. S, M. Mascalchi and A. R. Formiconi, "A Direct ROI Quantification Method for Inherent PVE Correction: Accuracy Assessment in Striatal SPECT Measurements". *European Journal of Nuclear Medicine and Molecular Imaging*, vol. 34-9, pp. 1480-89, 2007.

[32] A. P. Dempster, N. M. Laird and D. B. Rubin, "Maximum Likelihood from Incomplete Data via the EM Algorithm". *J Royal Stat Soc B*, vol. 38, pp. 11-38, 1977.

[33] L. A. Shepp and Y. Vardi, "Maximum Likelihood Reconstruction for Emission Tomography". *IEEE Trans. Med. Imag.*, vol. 1, pp. 113-122, 1982.

[34] C. Cloquet, "MLEM and OSEM Deviate From the Cramer-Rao Bound at Low Counts". *IEEE Trans. Nucl. Sc.*, vol. 60-1, pp. 134-143, 2013.

[35] E. T. P. Slijpen and F. J. Beekman, "Comparison of Post-filtering and Filtering Between Iterations for SPECT Reconstruction". *IEEE Trans. Nucl. Sci.*, vol. 46, pp. 2233-2238, 1999.

[36] B. W. Silverman et al, "A Smoothed EM Approach to Indirect Estimation Problems, with Particular Reference to Stereology and Emission Tomography". *Journal of the Royal Statistical Society, Series B*, vol 52-2, pp. 271-324, 1990.

[37] S. Mustafovic, K. Thielemans, D. Hogg and P. Bloomfield, "Object dependency of resolution and convergence rate in OSEM with filtering". *IEEE Nuclear Science Symposium Conference Record*, vol. 3, pp. 1786-1790, 2001.

[38] D. E. Knuth, "Seminumerical Algorithms. The Art of Computer Programming, Volume 2". *Addison Wesley*, 1969.

[39] H. Zaidi, "Quantitative Analysis in Nuclear Medicine Imaging". *Springer-Verlag*, New-York, 2006.

[40] M. Soret, P. M. Koulibaly, J. Darcourt, S. Hapdey and I. Buvat, **"**Quantitative Accuracy of Dopaminergic Neurotransmission Imaging with ^{123}I SPECT". *Journal of Nuclear Medicine*, vol. 44-7, pp. 1184-1193, 2003.